Numerical Analysis of Relaminarization in Turbulent Channel Flow

Sandeep Pandey, Cenk Evrim, and Eckart Laurien

Abstract The turbulent channel flow subjected to a wall-normal, non-uniform body force is investigated here by means of direct numerical simulations (DNS). The DNS is performed with the spectral/*hp* element solver, Nektar++. Flow relaminarization and turbulence recovery were observed in the body-force-influenced flow when compared to the flow at the same Reynolds number. The interaction events assist the recovery at higher body forces and result in two peaks in the ratio of production to dissipation of turbulent kinetic energy. The spectra of velocity fluctuations are also analyzed which shows a drastic reduction in the energy and stretched tail in the dissipation range during the relaminarization which indicates the disappearance of streaky structures in the flow. A retrieval in the energy was observed as a result of turbulence recovery at low wave numbers. The strong scaling characteristics of the employed computational code shows a good scalability.

1 Introduction

Turbulent fluid flows are one of the most challenging problem in physics but are common in engineering applications. The turbulent flow subjected to any kind of body-force may suffer from the modulated turbulence. The body force has the potential to distort the mean velocity profile [3]. There are several investigations made to unveil the effects of the body force on the fluid flow. The effects of the Lorenz force, which is a result of the magnetic field, is widely examined in the literature due to possibilities of flow control [9, 15]. The Lorentz force can suppress the near-wall turbulence structures and it can also result in drag reduction in electrically conduct-

S. Pandey · C. Evrim (✉) · E. Laurien
Institute of Nuclear Technology and Energy Systems, University of Stuttgart, Stuttgart, Germany
e-mail: cenk.evrim@ike.uni-stuttgart.de

S. Pandey
e-mail: sandeep.pandey@ike.uni-stuttgart.de

E. Laurien
e-mail: eckart.laurien@ike.uni-stuttgart.de

W. E. Nagel et al. (eds.), *High Performance Computing in Science and Engineering '19*,
https://doi.org/10.1007/978-3-030-66792-4_27

ing fluids [15]. Kühen et al. [12] made a successful attempt to reduce the drag by modifying the streamwise velocity profile so that the flow fully relaminarizes. This is achieved by enhancing turbulence mixing which created a more uniform mean flow [13]. Flow subjected to streamwise acceleration also shows similar characteristics of turbulence attenuation [14, 18]. Sreenivasan [24] categorized turbulent flow subjected to the different phenomenon (e.g. acceleration, suction, blowing, magnetic fields, stratification, rotation, curvature, heating, etc.) into three regimes, namely, laminarescence, relaminarization, and retransition.

The flow of supercritical CO_2 is affected by the body force due to the gravity, which influences the flow drastically [6, 20] and it is the main motivation for this work. Both forced and natural convection play here a significant role in the flow and heat transfer. The characteristics of body force on the mixed convection can catastrophically affect the turbulence in certain circumstances. In heated vertical flow, the direction of fluid flow dictates the nature of heat transfer [10]. In buoyancy aided flow (heated upward flow and cooled downward flow), body force can significantly enhance the skin friction coefficient and decrease the convective heat transfer coefficient as a result of the suppression in turbulence [23]. Flow can even become laminar under a strong buoyancy force. The velocity profile flattens out during the relaminarization [25]. Flow recovers with a different kind of turbulence with a further increase in the buoyancy force and the velocity profile acquires an 'M' shape. The transformation of velocity profile is due to the external effects of buoyancy resulting from the local flow acceleration close to the wall which compensates the decrease in velocity in the core [3, 22].

Pandey et al. [23] showed that the reduction in sweep and ejection events results in turbulence attenuation in downward flow under cooling condition, while the inward and outward interaction events are responsible for a recovery. Chu et al. [5] performed a DNS study to examine the role of buoyancy in a strongly heated air flow through a pipe subjected to a buoyancy force. They reported that buoyancy production is suppressed as compared to turbulent kinetic energy production during relaminarization. They also observed longer streaks near the wall which separated the pipe flow into two layers with an increased anisotropy in the near-wall layer. Chu and Laurien [4] conducted a DNS investigation for horizontal flow of CO_2 with flow heating to find out the effects of gravity. In this type of configuration, thermal stratification was noticed in which low-density fluid accumulates at the top of the pipe. Due to the body force at supercritical pressure, most of the simple models do not perform well [19, 21]. However, the new machine learning based models proved to be a good alternative [2, 7], where data from DNS can be used.

This study aims to enhance our knowledge in understanding the role of a body force on the flow turbulence. As a high-fidelity approach, direct numerical simulations are used for a canonical geometry of a channel with periodic boundary conditions. Special attention is given to the flow relaminarization induced by the body force. The present work also aims to investigate the spectra of turbulent energy during the flow relaminarization and flow recovery.

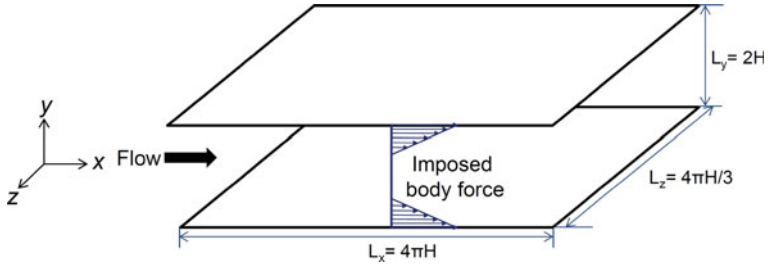

Fig. 1 Geometry for turbulent channel flow

2 Simulation Details

In the course of this project, different open source CFD codes have been used earlier. During this phase, a new CFD code is extended to analyze the effects of non-uniform body force. This section describes the governing equation, numerical method, computational details along with the supporting theory for the analysis.

2.1 Computational Domain and Boundary Conditions

An incompressible channel flow of a Newtonian fluid is considered here. The channel has the dimensions, $L_x \times L_y \times L_z = 4\pi H \times 2H \times 4\pi/3H$, where H is the half channel height as shown in Fig. 1. Periodic boundary conditions are used in the homogeneous streamwise (x) and spanwise directions (z) and no-slip boundary conditions are used at the two walls. The flow is driven by a temporally and spatially constant streamwise pressure gradient. The body force profile can take different shapes depending on the specific physical problem. Typically, the near-wall distribution of the body force results in a peculiar phenomenon. The primary aim of this work is to investigate the body-force-influenced flow at supercritical pressure. The density shows a steep variation due to the fact that temperature and pressure lie in the near-critical region. This density variation results in body force due to buoyancy (ρg). Therefore, a similar body force profile was employed in this work to resemble a buoyancy-aided-flow. Figure 2 illustrates the body force profile used in this work. Only the strength of the force was varied without considering its range of coverage. The body force here does not have exact quantitative variation similar to the buoyancy force in flow of sCO_2, rather its vary qualitatively. It also decouples the effects of variation in thermophysical properties which ultimately allow us to analyze the sole effect of body force.

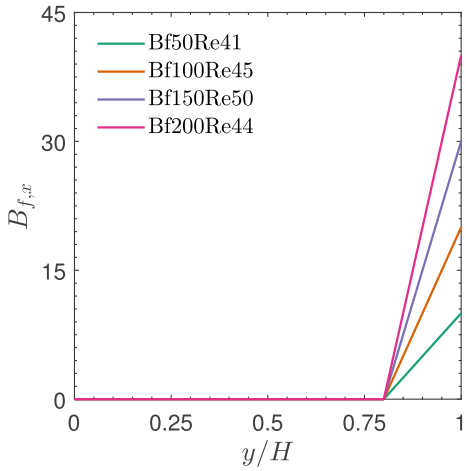

Fig. 2 Wall normal profile of body force employed in this work

2.2 *Governing Equations*

The flow governing equations are given in Eqs. 1–2. In these equations, **u** denotes the velocity vector, and p is the pressure. The viscous stress is denoted by τ and defined in Eq. 3.

$$\nabla \cdot (\mathbf{u}) = 0 \tag{1}$$

$$\frac{\partial \mathbf{u}}{\partial t} + \nabla \cdot [\mathbf{uu} + p\mathbf{I} - \tau] = \mathbf{B_f} \tag{2}$$

$$\tau = \mu\Big[[\nabla \mathbf{u} + (\nabla \mathbf{u})^T] - \frac{2}{3}(\nabla \cdot \mathbf{u})\mathbf{I}\Big] \tag{3}$$

A forcing term ($\mathbf{B_f} = [B_{f,x}, 0, 0]^T$) was added to the streamwise momentum equation. The forcing term remains constant throughout the domain and it is governed by Eq. 4.

$$B_f, x = \begin{cases} Ay, & if\ |y/H| > 0.8 \\ 0, & if\ |y/H| \leq 0.8 \end{cases} \tag{4}$$

Direct numerical simulations are performed with the spectral/*hp* element solver Nektar++ [1]. A velocity correction scheme was employed where the velocity system and the pressure are typically decoupled. Spatial discretization is based on the spectral element method in the y, z—plane combined with a Fourier decomposition in the x-direction. The time integration is treated using a second-order accurate mixed implicit-explicit (IMEX) scheme [11]. The simulation domain is discretized with a regular, structured quadrilateral mesh combined with eighth-order polynomials. This solver package has been used in many studies pertaining to fluid mechanics

Table 1 A summary of simulation conditions

Sr. Nr.	Case	Re_b	Re_τ	B_f	Δx^+	Δy^+_{min}-Δy^+_{max}	Δz^+
1	Bf50Re41	4190	256	B_f, x	8.0	0.15–2.5	5.8
2	Bf0Re41	4190	259	0	8.1	0.15–2.5	5.9
3	Bf100Re45	4565	266	B_f, x	8.3	0.15–2.7	6.1
4	Bf0Re45	4565	279	0	8.7	0.15–2.7	6.4
5	Bf150Re50	5000	310	B_f, x	9.7	0.15–3.1	7.1
6	Bf0Re50	5000	302	0	9.4	0.20–3.0	6.9
7	Bf200Re44	4490	337	B_f, x	10.5	0.20–3.3	7.7
8	Bf0Re44	4490	275	0	8.6	0.20–2.7	6.3

[8, 27]. The continuous Galerkin was selected for projection and advection was handled explicitly. The y,z- plane is discretized with 21 × 27 quadrilateral elements. The modified Legendre basis was used with eight modes (maximum polynomial order is 7). The streamwise direction contains 384 homogeneous modes. The streamwise mesh resolution normalized by the friction velocity ($\Delta x^+ = \Delta x u_\tau/\nu$) is kept below 10.5, and the dimensionless spanwise mesh resolution was below 7.7 in every case. The mesh was refined near to the wall and it has a maximum dimensionless spanwise mesh resolution 6.7 at the center and 0.4 at the wall. Table 1 shows the used resolutions for individual case. Spectral accuracy is one of the added advantage of using Nektar++ combined with high order nature of the code. The earlier work with OpenFOAM was having only second order of accuracy and finite volume implementation.

In the present study, eight distinct cases have been simulated, four of which include a varying body force and the remaining four are reference cases simulated without body forces, but with the same Reynolds numbers. These cases are selected to resemble a buoyancy-aided flow. Table 1 shows the parameters for all simulated cases. The bulk Reynolds number is defined as $Re_b = u_b H/\nu$, where ν is the kinematic viscosity and u_b is the bulk velocity. The body force, B_f follows a profile given by Eq. 4 and Fig. 2.

3 Results and Discussion

Direct numerical simulations were conducted for all eight cases mentioned in Table 1. Few important results are discussed here along with a code verification study. In this section, any generic quantity (say ϕ) is averaged in time as well as in streamwise and spanwise, and $\overline{\phi}$ shows the same while fluctuating part is shown as ϕ'.

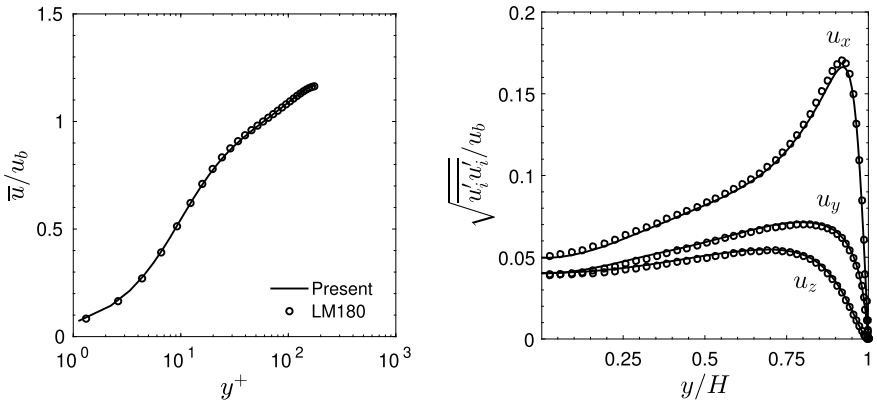

Fig. 3 Verification of the present DNS code with Lee and Moser [16]; **a**: mean streamwise velocity profile, **b**: root mean square fluctuations of velocity

3.1 Verification of the Code

The incompressible channel flow at a friction Reynolds number of 182 and a bulk Reynolds number of 2857 is verified with the well known incompressible channel flow DNS data of Lee and Moser [16] (acronym as LM180). The corresponding simulations were performed with the Nektar++ code. Figure 3 shows the wall-normal profiles for the mean velocity and the root mean square velocity fluctuations normalized with the bulk velocity (u_b). A very good agreement can be observed from Fig. 3 for the incompressible flow case.

The present study takes the advantage of the spectral analysis. Therefore, a verification study was also performed for the spectra as shown in Fig. 4 for $y^+ = 30$. The spectra is time-averaged and obtained by fast Fourier transform of the velocity fluctuations. The comparison is made between the classical DNS data of Moser et al. [17] (acronym as MKM) and a recent data from Vreman and Kuerten [26]. A good agreement can be seen for all three component of the velocity fluctuations.

3.2 Instantaneous and Mean Flow

The qualitative change of the flow field with increasing body forces is shown in Fig. 5, where the instantaneous streamwise velocity, normalized by bulk velocity, is depicted at one of the axial x-positions. With an increase in the body force, the contours change their shape. Relaminarization can clearly be visualized in Fig. 5b, corresponding to case Bf100Re45. With a stronger body force, a flow recovery can be seen in Fig. 5c, d. Also, it can be noticed from Fig. 5d that the fluid close to the

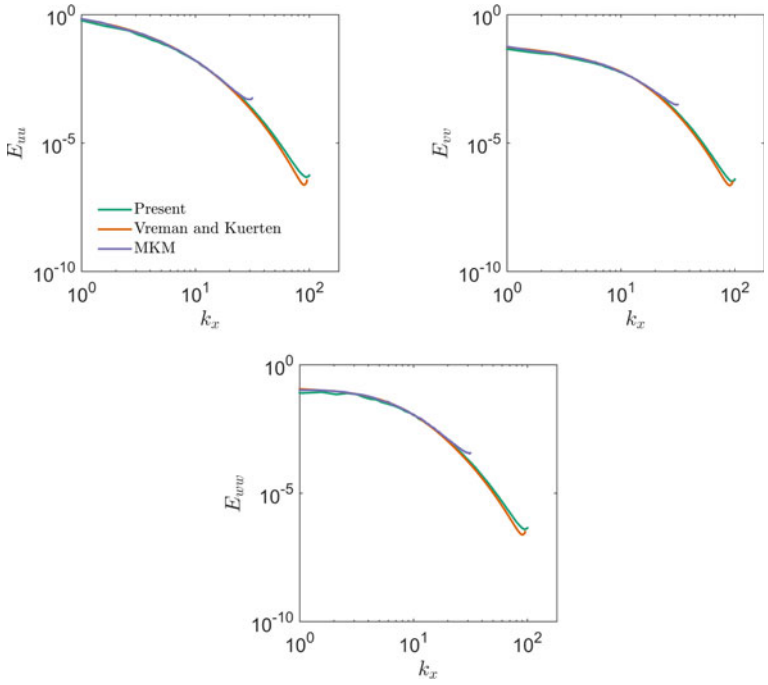

Fig. 4 Verification of the present DNS code with MKM and Vreman and Kuerten; **a**: E_{uu}, **b**: E_{vv}, and **c**: E_{ww} at $y^+ = 30$

wall, shows a higher velocity compared to the center in the recovered case which is contrary to Fig. 5a.

The temporal and spatial averaged streamwise velocity profile ($\overline{u}_x$) is shown in Fig. 6a in physical coordinates as well as in semi-logarithmic wall coordinates. As expected, the body force distorts the velocity profile. With a relatively low value of the body force (case Bf50Re41), the core velocity decreases to compensate the increased velocity near to the wall, as compared to the reference case. With further increasing body force (case Bf100Re45), the velocity profile flattens out and flow relaminarization was observed. The flow recovers as soon as the body force increases further and the velocity profile shows its typical 'M'-shape. The 'M'-shape profile in the channel flow is the effect of (strong) wall jets near each wall. Long and strong wall jets lead to an inflection point in the respective boundary layer and to a strong inviscid instability that holds for laminar as well as turbulent flow. It results in a second strong peak in the production of turbulent kinetic energy, which is discussed latter. The wall normal gradient of the streamwise velocity also varies with an increase in the body force as shown in Fig. 6b. The velocity gradient adjacent to the wall increases with

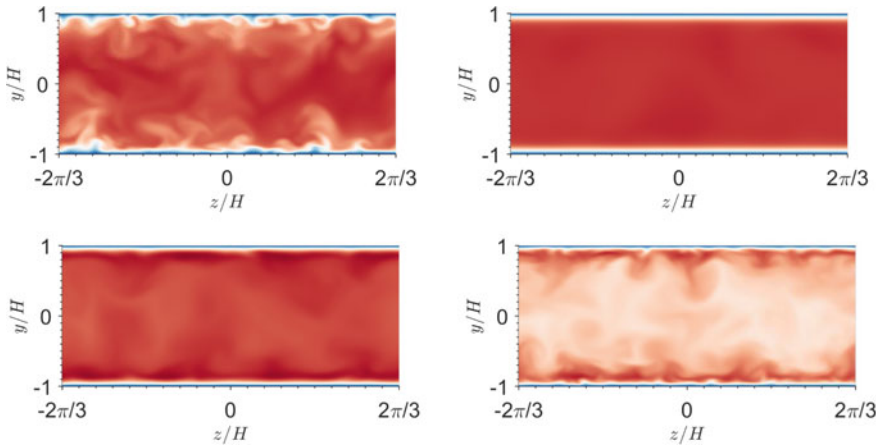

Fig. 5 Pseudo-colour visualization of the instantaneous streamwise velocity u_x, normalized by the bulk velocity u_b. **a**, **b**, **c**, **d**: Case 1,3,5, and 7 respectively

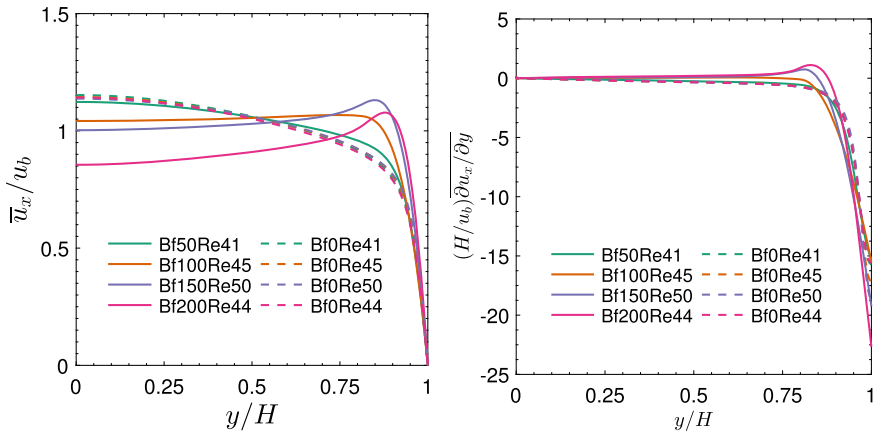

Fig. 6 Distribution of **a**: mean velocity profile, **b**: wall normal streamwise-velocity gradient

growing in body forces. Thus, positively affects the wall shear stress and thereby, the friction Reynolds number (as can be seen in Table 1). Due to the 'M'-shape profile, the mean shear rate increases close to the wall as a result of a local flow acceleration close to the wall. This assists a turbulence recovery by positively affecting the turbulence production. It can also be observe that the body force reduces the fluctuation until flow laminarize. The strength of streaks is significantly reduced in case Bf100Re45 (laminarized) and case Bf150Re50 (partially recovered). This certainly breaks the self-sustaining process and will result in elongated streaks in the near-wall region.

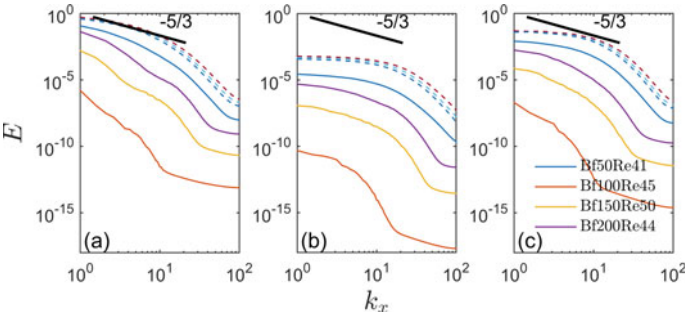

Fig. 7 One-dimensional spectra of **a**: E_{uu}, **b**: E_{vv}, and **c**: E_{ww} at $y/H = 0.99$. Dashed lines shows the reference case

3.3 Spectral Analysis

The streamwise turbulence energy spectra are analyzed in this section to investigate an inconsistent behavior due to the body force. Figure 7 illustrates the one-dimensional spectra for all three velocity components at $y/H = 0.99$ for both reference and body-force-influenced case. The reference case shows an expected behavior with fluctuating energies (E) of all velocity components, which decreases monotonically with an increase in streamwise wave number (k_x). An increase in the body force attributes to a reduction in energy. Due to the turbulence recovery, a retrieval in energy can also be seen at the low wave numbers. Interestingly, the energy containing range vanished out in the spectra of the streamwise velocity for the relaminarized case (case Bf100Re45) as shown Fig. 7a. Also, the tail of the spectra at high wave numbers is stretched out. Figure 8 shows the spectra at $y/H = 0.90$ for both reference and body-force-influenced case. It also shows a similar behavior with a drastic reduction in energy and a stretched tail in the dissipation range. Even after the recovery, this tail remains in the spectra, however, in a shorter range. As mentioned earlier, the recovery was contributed by the 'M' shape velocity profile which is associated with the positive turbulent production.

The drastic reduction in the energy at low wave numbers associated with the relaminarization can be explained by the ratio of production $\left(P_k = -\overline{u_i' u_j'} \frac{\partial u_i}{\partial x_j}\right)$ to dissipation $\left(\varepsilon_k = -\nu \overline{\frac{\partial u_i}{\partial x_j} \frac{\partial u_i}{\partial x_j}}\right)$ of turbulent kinetic energy and it is shown in Fig. 9. The low body force case (case Bf50Re41) shows a typical behavior observed at low Reynolds numbers with a peak in the buffer layer. This peak vanishes during the relaminarization due to negligible turbulence production. It leads to a reduced energy density along with a vanished energy containing range observed in Figs. 7 and 8. When the recovery starts in case Bf150Re50, two peaks appear in the ratio (see Fig. 9). A strong peak is located between the center and the wall of the channel while a weak peak is close to the wall. The strong peak is the result of the interaction events of the Reynolds shear stress. These events shift towards the wall

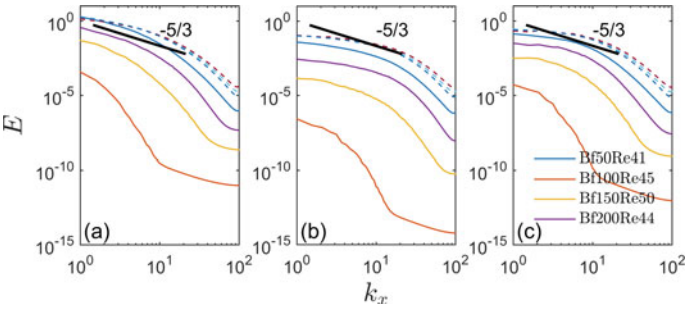

Fig. 8 One-dimensional spectra of **a**: E_{uu}, **b**: E_{vv}, and **c**: E_{ww} at $y/H = 0.90$. Dashed lines shows the reference case

Fig. 9 Distribution of the ratio of production to dissipation of turbulent kinetic energy

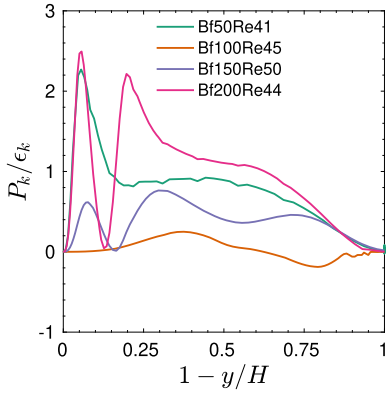

in the recovery (case Bf200Re44) which results in the second peak much closer to the wall. In this case, another peak with the same strength also appears at the usual location (buffer layer) which is an outcome of sweep and ejection events which take place in this region.

3.4 Computational Performance

In this section, we present strong scaling characteristics of the code without multi-threading. The computational code used in this study, Nektar++, is based on the spectral/ *hp* element framework. It is a tensor product based finite element package programmed in C++. The code is parallelized by OpenMP and for this study, HDF5 format was employed for IO. Fourier modes was use in the homogeneous stream-wise direction, which allow a pseudo-3D simulations and reduces the computational effort compared to pure-3D simulation without loosing any generality. The simulations were performed on *Hazel Hen* located at the High-Performance Computing

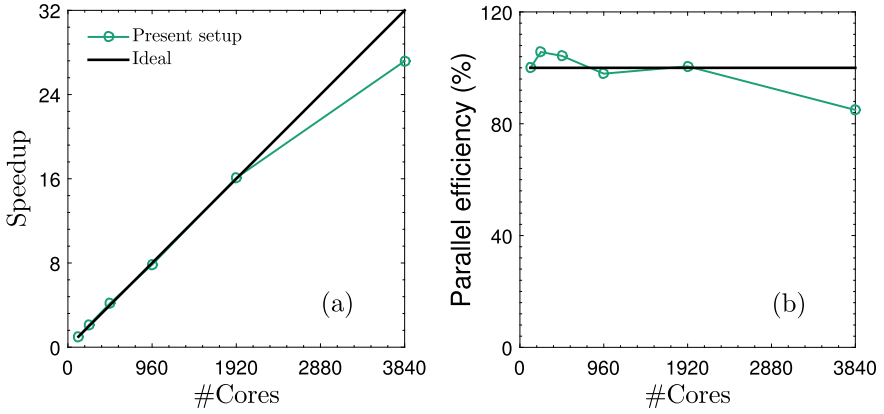

Fig. 10 Comparison of strong scaling of the present solver without multi-threading for a given ratio of number of cores to the number of partitions in the streamwise direction; **a** speedup **b** parallel-efficiency

Center (HLRS) Stuttgart for a range of 120–7680 physical cores. To demonstrate the computational performance, a strong scaling test was performed on *Hazel Hen*. For this purpose, the testcase has a maximum polynomial order of 4 and 768 modes in the streamwise direction. The degree of freedom for this testcase is approximately 60 Million. Typically, in our DNS, we have large number of Fourier modes in the homogeneous direction and relatively few elements in the y, z-plane. Therefore, it is more efficient to parallelize in the streamwise direction and this code allow us to do so by specifying a separate flag by which a single core handles particular modes.

Figure 10 illustrates the result from the strong scaling test. The curve shows the scaling when the ratio of number of cores to the number of partitions in the streamwise direction is constant (10 in this case). A very good scalability of the code can be seen until 1920 computational cores with a parallel efficiency up to 100%. Interestingly, there is a super-linear speed-up between 350 and 1920 cores. If we further double the number of cores then our performance degrades (not shown here). It is due the fact that for a given number of partitions, with the increase in the cores, the number of elements per cores decreases which creates an imbalance between computational time and communication time. In the future, we intend to seek the answers for influence of body force at higher Reynolds number, where the mesh resolution would be much higher due to the requirement for resolving Kolmogorov scale. The future work will require a mesh size of approximately 800 Million where it is expected to have a linear scaling even at higher nodes.

3.5 Conclusion

In this work, a systematic study of body-force-influenced flow in a channel has been performed by means of direct numerical simulations. The DNS are performed with a spectral/*hp* element method. A wall-normal varying body force was added to the streamwise momentum equation to elucidate the effects on turbulence. The body force influences the Reynolds numbers, therefore, additional simulations were also performed at the same Reynolds number without body force. The body force profile was motivated from the buoyancy force in supercritical fluids and have different strengths which allowed to observed all three possible states in such flows, viz., laminarescent (i.e. precursor of relaminarization), relaminarizing and recovery. The body force influences the mean velocity profile, thereby, affecting the gradient of the mean velocity which ultimately modulates the turbulence production. Two peaks in the ratio of production to dissipation of turbulent kinetic energy were observed during the recovery as a result of interaction events. The streamwise spectrum of the streamwise velocity fluctuations depicted a drastic reduction in energy and a stretched tail in the dissipation range along with a vanished energy containing range. This occurred due to a negligible production which itself was the result of flow relaminarization. The strong scaling of the computational code shows a good scalability even with a low degree of freedom. In the future, we intend to use much higher degree of freedom to analyze the flow at high Reynolds number.

Acknowledgements The authors are sincerely thankful to the High Performance Computing Center (HLRS) Stuttgart for providing access to *Hazel Hen* under project DNSTHTSC. SP is grateful to the Forschungsinstitut für Kerntechnik und Energiewandlung (KE) e.V., Stuttgart, for the fellowship. We are also thankful to the anonymous reviewers for his/her valuable suggestion on some of the technical aspects of this report.

References

1. C. Cantwell, S. Sherwin, R. Kirby, P. Kelly, From h to p efficiently: strategy selection for operator evaluation on hexahedral and tetrahedral elements. Comput. Fluids **43**(1), 23–28 (2011)
2. W. Chang, X. Chu, A.F.B.S. Fareed, S. Pandey, J. Luo, B. Weigand, E. Laurien, Heat transfer prediction of supercritical water with artificial neural networks. Appl. Therm. Eng. **131**, 815–824 (2018)
3. X. Chu, E. Laurien, Direct numerical simulation of heated turbulent pipe flow at supercritical pressure. J. Nucl. Eng. Radiat. Sci. (2) (2016)
4. X. Chu, E. Laurien, Flow stratification of supercritical CO2 in a heated horizontal pipe. J. Supercrit. Fluids **116**, 172–189 (2016)
5. X. Chu, E. Laurien, D.M. McEligot, Direct numerical simulation of strongly heated air flow in a vertical pipe. Int. J. Heat Mass Transf. **101**, 1163–1176 (2016)
6. X. Chu, E. Laurien, S. Pandey, Direct Numerical Simulation of Heated Pipe Flow with Strong Property Variation (Springer International Publishing, 2016), pp. 473–486

7. X. Chu, W. Chang, S. Pandey, J. Luo, B. Weigand, E. Laurien, A computationally light data-driven approach for heat transfer and hydraulic characteristics modeling of supercritical fluids: From DNS to DNN. Int. J. Heat Mass Transf. **123**, 629–636 (2018)
8. X. Chu, G. Yang, S. Pandey, B. Weigand, Direct numerical simulation of convective heat transfer in porous media. Int. J. Heat Mass Transf. **133**, 11–20 (2019)
9. C.H. Crawford, G.E. Karniadakis, Reynolds stress analysis of EMHD-controlled wall turbulence. Part I. Streamwise forcing. Phys. Fluids **9**(3), 788–806 (1997)
10. J. Jackson, M. Cotton, B. Axcell, Studies of mixed convection in vertical tubes. Int. J. Heat Fluid Flow **10**(1), 2–15 (1989)
11. G.E. Karniadakis, M. Israeli, S.A. Orszag, High-order splitting methods for the incompressible Navier–Stokes equations. J. Comput. Phys. **97**(2), 414–443 (1991)
12. J. Kühnen, D. Scarselli, M. Schaner, B. Hof, Relaminarization by steady modification of the streamwise velocity profile in a pipe. Flow Turbul. Combust. **100**(4), 919–943 (2018)
13. J. Kühnen, B. Song, D. Scarselli, N.B. Budanur, M. Riedl, A.P. Willis, M. Avila, B. Hof, Destabilizing turbulence in pipe flow. Nat. Phys. **14**(4), 386–390 (2018)
14. B. Launder, Laminarization of the turbulent boundary layer in a severe acceleration. J. Appl. Mech. **31**(4), 707–708 (1964)
15. D. Lee, H. Choi, Magnetohydrodynamic turbulent flow in a channel at low magnetic Reynolds number. J. Fluid Mech. **439**, 367–394 (2001)
16. M. Lee, R.D. Moser, Direct numerical simulation of turbulent channel flow up to $Re_\tau \approx 5200$. J. Fluid Mech. **774**, 395–415 (2015)
17. R.D. Moser, J. Kim, N.N. Mansour, Direct numerical simulation of turbulent channel flow up to $Re_\tau = 590$. Phys. Fluids **11**(4), 943–945 (1999)
18. R. Narasimha, K. Sreenivasan, Relaminarization in highly accelerated turbulent boundary layers. J. Fluid Mech. **61**(3), 417–447 (1973)
19. S. Pandey, E. Laurien, Heat transfer analysis at supercritical pressure using two layer theory. J. Supercrit. Fluids **109**, 80–86 (2016)
20. S. Pandey, X. Chu, E. Laurien, Investigation of in-tube cooling of carbon dioxide at supercritical pressure by means of direct numerical simulation. Int. J. Heat Mass Transf. **114**, 944–957 (2017)
21. S. Pandey, E. Laurien, X. Chu, A modified convective heat transfer model for heated pipe flow of supercritical carbon dioxide. Int. J. Therm. Sci. **117**, 227–238 (2017)
22. S. Pandey, X. Chu, E. Laurien, Numerical analysis of heat transfer during cooling of supercritical fluid by means of direct numerical simulation, in *High Performance Computing in Science and Engineering ' 17*, ed. by W.E. Nagel, D.H. Kröner, M.M. Resch (Springer International Publishing, Cham, 2018), pp. 241–254
23. S. Pandey, X. Chu, E. Laurien, B. Weigand, Buoyancy induced turbulence modulation in pipe flow at supercritical pressure under cooling conditions. Phys. Fluids **30**(6), 065,105 (2018)
24. K.R. Sreenivasan, Laminarescent, relaminarizing and retransitional flows. Acta Mech. **44**(1), 1–48 (1982)
25. A. Steiner, On the reverse transition of a turbulent flow under the action of buoyancy forces. J. Fluid Mech. **47**(3), 503–512 (1971)
26. A.W. Vreman, J.G.M. Kuerten, Comparison of direct numerical simulation databases of turbulent channel flow at $Re_\tau = 180$. Phys. Fluids **26**(1), 015,102 (2014)
27. H. Xu, S.M. Mughal, E.R. Gowree, C.J. Atkin, S.J. Sherwin, Destabilisation and modification of Tollmien–Schlichting disturbances by a three-dimensional surface indentation. J. Fluid Mech. **819**, 592–620 (2017)